RESEARCH PAPER

Effects of particle sphericity and initial fabric on the shearing behavior of soil–rough structural interface

Wan-Huan Zhou[1,2] · Xue-Ying Jing[1] ⓘ · Zhen-Yu Yin[3] · Xueyu Geng[4]

Abstract

In this study, the effects of particle sphericity and initial fabric on the shearing behavior of soil-structural interface were analyzed by discrete element method (DEM). Three types of clustered particles were designed to represent irregular particles featuring various sphericities. The extreme porosities of granular materials composed of various clustered particles were affected by particle sphericity. Moreover, five specimens consisting of differently oriented particles were prepared to study the effect of initial fabric. A series of interface shear tests featuring varying interface roughnesses were carried out using three-dimensional (3D) DEM simulations. The macro-response showed that the shear strength of the interface increased as particle sphericity decreased, while stress softening and dilatancy were easily observed during the shearing. From the particle-scale analysis, it was found that the thickness of the localized band was affected by the interface roughness, the normal stress and the initial fabric while independent of the particle sphericity. The thickness generally ranged between 4 and 6 times that of the median particle equivalent diameter. A thicker localized band was formed in the case of rougher interface and in soil composed of inclined placed and randomly placed particles. The coordination number measured in the interface zone and upper zone suggested that the dilation mostly occurs inside the interface zone. Anisotropy was induced by the interface shearing of the initial isotropic specimens. The direction of shear-induced anisotropy correlates with the shearing direction. The evolutions of anisotropies for the anisotropic specimens depend on the initial fabric.

1 Introduction

The soil-structural interface (SSI) is involved in many aspects of geotechnical engineering. The conventional research studies that characterize the mechanical behavior of SSI commonly rely on laboratory-based and on-site experiments. Certain valuable phenomena have been observed and have provided a fundamental understanding of the SSI issue [15, 16, 29, 30, 36, 41, 49, 51–53]. Efforts have been made to investigate the influencing factors in the mechanical behavior of SSI. The laboratory experiments found that the interface roughness affects the shear resistance and volumetric change of soil shearing at interface [9, 12, 28, 37, 38, 50]. In addition, the numerical simulations reveal that the interface roughness is involved in the stress–strain evolution pattern as well as the strain localization inside soil shearing at an interface [10, 14, 42].

✉ Xue-Ying Jing
  jingxueying73@gmail.com

1   Department of Civil and Environmental Engineering, Faculty of Science and Technology, University of Macau, Macau, China

2   Zhuhai UM Science and Technology Research Institute, Zhuhai, Guangdong, China

3   Department of Civil and Environmental Engineering, Hong Kong Polytechnic University, Hung Hom, Kowloon, Hong Kong, China

4   Geotechnical Engineering School of Engineering (F332), The University of Warwick, Coventry CV4 7AL, UK

Furthermore, both the shear resistance and volumetric change of the SSI depend on the soil properties [11, 26, 47]. For example, the initial relative density determines whether the soil dilates or contracts [9, 54], and the shear strength of bulk soil governs the shear resistance ability at the interface [12, 43].

A rich body of investigations has proved that the grain shape emerges as an essential soil property that affects the various mechanical behaviors of bulk soil. The relationship between the compactness of the soil and the shape parameter has been exploited in terms of the maximum and minimum void ratio [23, 24]. The motions of the particles, including movement and rotation, result in the macroscopic deformation of a granular system. The rotation of a particle with an irregular shape is restricted and accordingly increases the interlocking inside the soil, leading to a higher shear strength and a larger dilation [34]. Moreover, the shear-induced anisotropy of a granular material composed of non-spherical particles is emphasized due to the particle eccentricity [27, 32]. In this context, the particle shape emerges as an essential soil property that needs to be properly considered in the SSI issue. The particle shape is generally characterized using three scales: roundness, sphericity, and smoothness [19]. The sphericity S is correlated to the rotation of the particle and the arrangement of the granular material, which are crucial to the macroscopic behaviors of the granular material. Thus, this study will focus on the effects of particle sphericity. Furthermore, the orientations of irregular particles will lead to an initial anisotropy of the specimen [4, 48]. Thus, the effect of initial fabric on SSI shearing behavior should be discussed as well.

The discrete element method (DEM) as a numerical tool has been widely used in the geotechnical field due to the fact that soil is discontinuous in nature. Two-dimensional (2D) and three-dimensional (3D) DEM simulations have been successfully applied in the soil-structure interface issue [10, 18 14, 43]. The particle used in the early DEM models was a disk in the 2D case and a spherical particle in the 3D case. Certain methods have been proposed to mimic the behavior of a non-spherical particle in DEM simulation. For example, the rolling resistant contact law between spherical particles has been proposed to manually prevent the rotation of particles by introducing a rolling friction coefficient [1, 13, 44]. However, real soil particles are generally with various shapes, different from idealized granular system with disks and spherical particles, which significantly affects the mechanical behavior of soils. For this reason, non-spherical elements have been successfully applied in DEM simulation, such as clustered particles, polygons, and ellipsoids [3, 20, 21, 25, 33]. Jensen et al. [14] employed a clustered element in 2D simulation of IST. However, how the shear resistance, material fabric, and particle motions are affected by the particle sphericity and initial fabric during interface shearing has not been fully studied. Furthermore, the thickness of localized band should be measured under various loading and modeling conditions.

In this study, the effect of particle shape was thoroughly investigated by 3D DEM. Different types of clustered particles were used to represent the irregular particles with various sphericities. Specimens were randomly generated and sheared on interfaces with different roughnesses. Based on the DEM interface shear test results, the following 4 aspects were explored: (1) the effect of particle sphericity on extreme porosities of granular material, (2) the effect of particle sphericity on both macro- and micro-shearing behaviors of SSI, (3) the effect of interface roughness on the behaviors of SSI and (4) the effect of initial fabric on the shearing behaviors of SSI.

2 The DEM simulation

2.1 Input parameters

PFC 3D 5.0 software based on the discrete element method proposed by [8] was employed in this study. The Hertz–Mindlin contact law was used to describe the nonlinear force–displacement relationship between two contacting particles [22]. The shear modulus G and Poisson's ratio v were used to describe the deformability of the granular material. The values of the input parameters used in this study refer to the 3D simulation performed by Lin and Ng [20] using arrays of ellipsoids, in which the shear modulus G was 28.957 GPa, the Poisson's ratio v was 0.15 and the inter-particle friction coefficient μ_p was 0.5. A damping coefficient with a value of 0.7 was applied to dissipate the energy together with the sliding and guarantee a quasistatic analysis.

2.2 Geometries of the clumps

A clustered particle, named clump, can be formed by adding certain particles together with or without overlapping. Efforts were made to bring the geometry of the clump close to that of real sand grain by composing more particles with the help of a 3D scanning technique or specific algorithms. Those sophisticated approaches validated the significance of the particle shape in the DEM simulation but created another problem. It was time-consuming, because of the remarkably increased particle numbers, to form a clustered element that would be closer to the real one. It has been asserted that a clump having asymmetry geometry is sufficiently close to the mechanical behavior of

real soil material. Thus, clumps composed of two or three single particles were enough for the simulation, which took into account the effect of particle shape [7, 33].

The sphericity S is characterized as shown in Fig. 1a [19]. The r_{max_in} is the radius of the maximum inscribed sphere, and the r_{min_cir} is the radius of the minimum circumscribed sphere of the irregular particle. The clumps, composed of different numbers of spherical particles representing various sphericity S used in the model, are named C1, C2, C3, and C4, respectively (Fig. 1b).

2.3 Specimen generation process

The specimen preparation method refers to the procedure proposed by Wood and Maeda [45] to obtain a granular material with varied porosity n (Fig. 2). The specimen followed a given particle-size distribution, and a specific initial porosity n_0 was randomly generated inside a container with six frictionless walls. To obtain the densest granular material, the initial friction coefficient between particles μ_{p0} was set to zero and the initial porosity n_0 of the specimen was set to 0.2. Overlapping particles immediately spread out or separated to achieve an equilibrium state. Then the walls of the container were controlled by a servo system until the mean stress on the walls reached a given value σ_0 by moving slowly inward or outward. The friction coefficient of particle μ_{p0} changed to the eventual value μ_p and was maintained as a constant in the shearing stage. Then the final porosity of the specimen regained the equilibrium state, which was defined as the minimum porosity n_{min}. In contrast, to obtain a "loosest" specimen, the initial friction coefficient of particle μ_{p0} was set to 1.0 to generate a specimen with a high n_0 equals 0.4. Then the same procedure was performed to obtain the loosest sample. The eventual porosity n of the granular material can be altered by inputting a different value of μ_{p0} and n_0.

2.4 The simulation of soil–rough interface shearing

The numerical model of soil–rough interface shear test is illustrated in Fig. 3. The dimension of the shear box is described using length (L), width (W), and height (H). A regular saw-tooth wall is used in the model with an inclined angle θ equals $45°$ and a depth of each valley h. The normalized roughness R_n of this continuum interface is defined as h/d_{50} referring to the definition proposed by Uesugi and Kishida [39], where d_{50} is the mean particle diameter. The value of R_n is 0.5 in the following simulations. Four specimens consisting of clumps C1, C2, C3, and C4, respectively, have been generated with a desired porosity n. Equivalent diameter d_{eq} is denoted for the clumps with a non-spherical shape, which is defined as the diameter of a spherical ball with the same volume as the clump. All specimens follow a same linear grain size distribution. The value of d_{eq} ranges between 1.8 and 3.6 mm, and the $d_{50(eq)}$ equals 2.7 mm.

Once the granular material reached an equilibrium state, a constant normal stress σ_n was applied on the top wall. The bottom rough interface wall began to move horizontally in x-direction at a low speed once the granular system was stabilized. The four lateral walls were fixed, and the top wall was vertically moveable during the shearing loading process. The top wall was controlled by a servo system to maintain a constant normal stress.

The macroscopic mechanical behaviors were measured according to the displacements and forces of the walls. The shear stress τ was the shear force measured on the interface wall divided by the area of horizontal section of the shear box. The shear displacement d_s was the displacement of the bottom wall in the direction of shearing. The normal stress σ_n was measured on the top wall. The vertical displacement
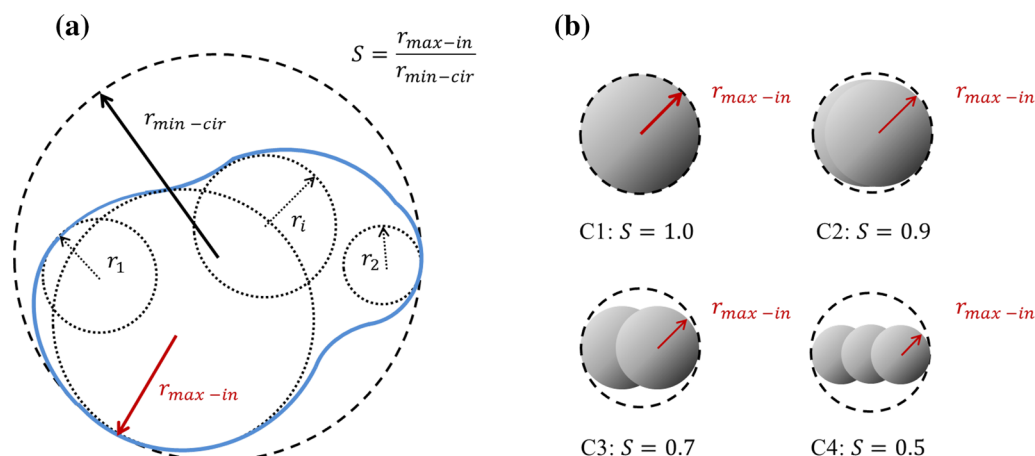

Fig. 1 **a** Definition of the sphericity S (Krumbein and Sloss [19]); **b** clumps used in this study
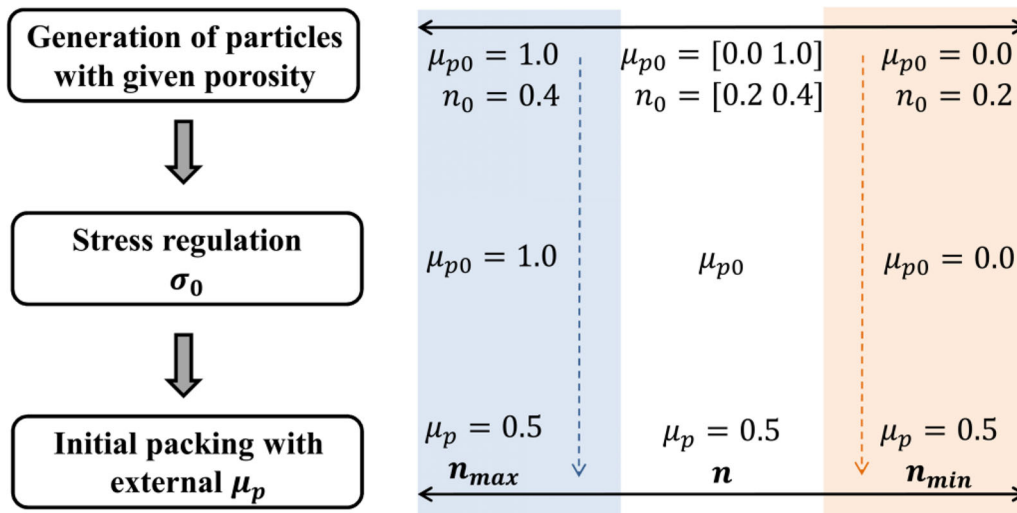
Fig. 2 Specimen generation procedure after Wood and Maeda [45]
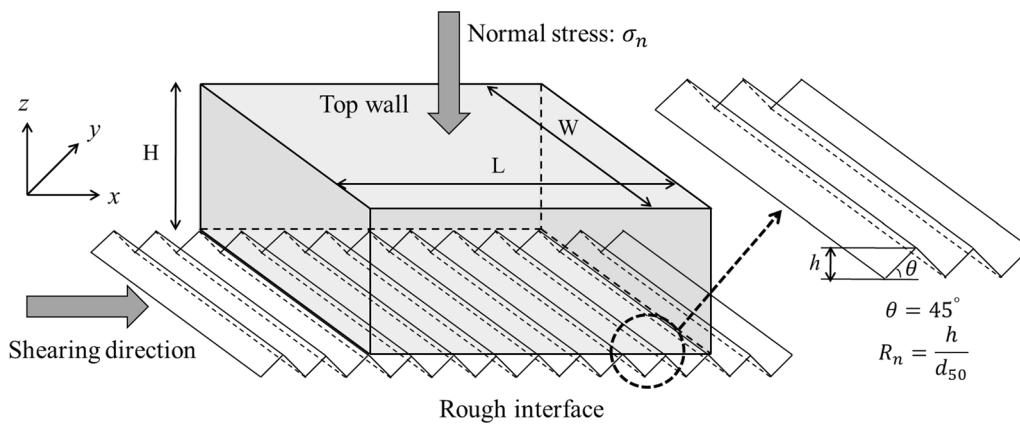

Fig. 3 Schematic diagram of interface shear test in the DEM simulation

d_v of the top wall was recorded to reflect the volumetric change of the specimen.

3 The compactness of the specimen

In this study, the maximum porosity n_{max} and minimal porosity n_{min} of a specimen composed of different clumps were obtained using the procedure introduced in Sect. 2.3. The values of n_{max} and n_{min} of various specimens are illustrated in Fig. 4, which shows that the specimen composed of spherical particles ($S = 1.0$) tends to form a loose configuration. Non-spherical particles allow a better filling of the void space compared to spherical particles, and as a result, a dense packing is achieved for the specimen with a smaller value of S. On the other hand, rolling easily occurs with spherical particles ($S = 1.0$) and leads to a similar configuration of the granular assembly at the loosest and densest configurations. Accordingly, the difference
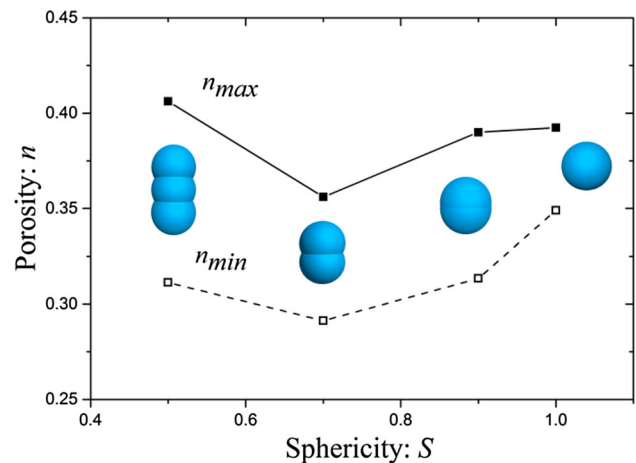

Fig. 4 The extreme porosities n_{max} and n_{min} of the specimen featuring various sphericity S

between the n_{max} and n_{min} for the specimen with spherical particles ($S = 1.0$) is smaller than the others with irregular

particles. It should be noted that the most elongated clump ($S = 0.5$) can form a structure with more void space and correspondingly results in a higher value of n_{max}. As mentioned by Salot et al. [33], the extreme porosities obtained in the numerical simulation cannot compare directly with those obtained in the experimental tests because of the difference in preparation procedure. However, it is necessary to control the relative density of the granular material when taking into account the particle shape effect in the DEM tests.

4 Effect of particle shape and interface roughness

The relative density D_r of the granular material is calculated by

$$D_r = \frac{(n_{max} - n)(1 - n_{min})}{(n_{max} - n_{min})(1 - n)} \quad (1)$$

Four specimens consisting of spheres and three types of clumps were generated, named $S1$, $S2$, $S3$, and $S4$, respectively. Each specimen comprised around 30,000 spheres or clumps. The dense configuration was guaranteed by controlling the $D_r = 90\%$ for all specimens. The desired initial porosities n_0 of each specimen were derived according to eq. (1) as listed in Table 1. To demonstrate the

Table 1 Summary of the numerical tests with various elements

Specimen	Sphericity	Normalized roughness of interface: R_n	Initial porosity: n_0
S1	$S = 1.0$	0.1	0.359
		0.25	0.353
		0.5	0.355
		0.75	0.352
		1.0	0.357
S2	$S = 0.9$	0.1	0.325
		0.25	0.329
		0.5	0.326
		0.75	0.322
		1.0	0.321
S3	$S = 0.7$	0.1	0.306
		0.25	0.309
		0.5	0.301
		0.75	0.297
		1.0	0.297
S4	$S = 0.5$	0.1	0.323
		0.25	0.326
		0.5	0.323
		0.75	0.325
		1.0	0.325

effect of particle sphericity on the macroscopic mechanical behavior of the SSI, sixty ISTs of specimen S1/2/3/4 shear on a rough interface featuring $R_n = 0.1/0.25/0.5/0.75/1.0$ under a normal stress σ_n equals 25 MPa/50 MPa/100 MPa respectively were modeled. The generation procedure is presented in Sect. 2.3.

4.1 Macroscopic response

The macroscopic mechanical behaviors of the ISTs comprising particles of various S are illustrated in Fig. 5 in terms of the stress ratio τ/σ_n and the vertical displacement d_v as a function of shear displacement d_s. As shown in Fig. 5a, the evolutions of τ/σ_n of the four tests display a similar tendency. Stress softening occurs once the τ/σ_n peaks. Note that the peak shear stress at the interface is affected by particle sphericity S. The specimens composed of non-spherical particles show a higher peak shear stress than one composed of spherical balls ($S = 1.0$). The difference in shear resistance is attributed to the interlocking phenomenon between the particles. Unlike the way a spherical particle easily rotates when making contact with another one, an irregular particle tends to interlock with other particles or the rough interface. The evolution of vertical displacement of the top wall d_v reflects the volumetric change in the specimen, showing that all specimens contract at the beginning of shearing and then gradually dilate. The growing rate of dilation slows down at shear displacement d_s where shear stress softening appears. This suggests that the volumetric change in the specimen is also affected by the particle sphericity. A larger dilatancy can be observed in the specimen with non-spherical particles. From the perspective of micro-mechanics, the volumetric change of a granular material is the result of the micro-physics of individual particles, i.e., movement and rotation. To help explain the macroscopic responses we obtained in the simulations, the micro-physics of the particles will be analyzed in the following sections.

The macroscopic mechanical behaviors of the ISTs ($S = 0.5$) featuring varying R_n under $\sigma_n = 50$ MPa are illustrated in Fig. 6. As shown in the figure, the peak shear stress ratio and volumetric change are affected by the R_n. A higher peak shear stress and larger dilation are observed when the specimen shearing on a rougher interface. This result is consistent with the existing experimental findings [12, 28], the shear strength of interface generally increases as the increasing of R_n. Note that periodic oscillation is observed in the curve of τ/σ_n when $R_n = 0.25$. In this case, the clumps in the bottom layer cannot fit into such small volumes between sawteeth. Thus, the bottom layer of clumps moves alternately between the tops of the teeth and the areas between teeth, which results in periodic
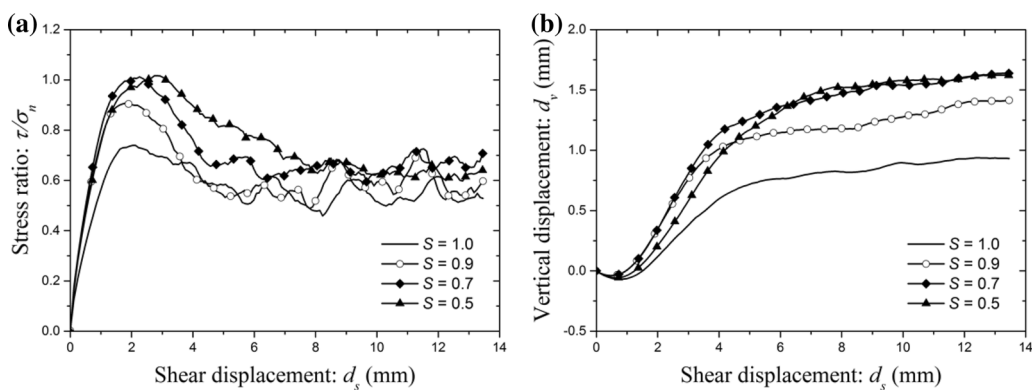
Fig. 5 Macroscopic responses of the ISTs comprising particles of various S ($D_r = 90\%$, $R_n = 0.5$, $\sigma_n = 50$ MPa): **a** stress ratio τ/σ_n versus shear displacement d_s; **b** vertical displacement d_v versus shear displacement d_s
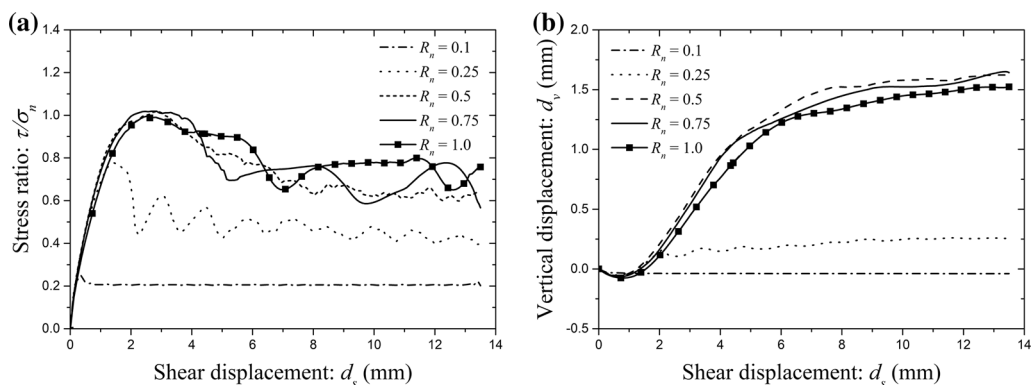

Fig. 6 Macroscopic responses of the ISTs ($S = 0.5$, $\sigma_n = 50$ MPa) featuring varying normalized roughness R_n: **a** stress ratio τ/σ_n versus shear displacement d_s; **b** vertical displacement d_v versus shear displacement d_s

oscillation in the total contact number between the bottom clumps and interface. This induces this kind of evolution of τ/σ_n.

4.2 Interface friction angle analysis

The peak shear stress τ_p and steady shear stress τ_s (at $d_s = 13.5$ mm) were obtained for the ISTs under various

normal stress 25 MPa/50 MPa/100 MPa. According to the Mohr–Column criterion, the peak friction angle ϕ_p and steady friction angle ϕ_s can be obtained by linearly fitting the τ_p and τ_s under various normal stress conditions (Fig. 7a, b). The cohesive force was assumed to be zero since a non-cohesive soil was considered in this study.

The friction angles of all ISTs are obtained by this criterion to discuss the effects of S and R_n on the shear
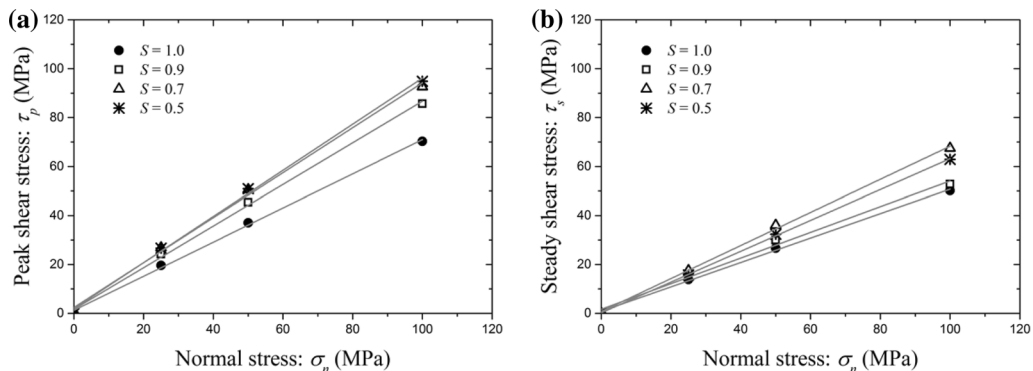

Fig. 7 **a** Fitting the peak shear stress τ_p as a function of normal stress σ_n; **b** fitting the steady shear stress τ_s as a function of normal stress σ_n ($R_n = 0.5$)

Table 2 Summary of the peak friction angles of ISTs and DSTs

Sphericity	Peak friction angle (°)					
	$R_n = 0.1$	$R_n = 0.25$	$R_n = 0.5$	$R_n = 0.75$	$R_n = 1.0$	DST
$S = 1.0$	11.89	21.70	35.51	36.07	34.85	35.74
$S = 0.9$	12.54	26.10	41.10	40.89	38.02	43.84
$S = 0.7$	13.14	30.15	43.53	45.05	41.48	49.42
$S = 0.5$	13.18	34.53	44.05	45.06	43.19	47.30

resistance of SSI. As a reference, the direct shear tests (DSTs) with the same input parameters under σ_n equals 25 MPa/50 MPa/100 MPa are modeled. The height of the interface shear box is twice of the specimen in IST. The peak friction angles of ISTs (ϕ_p) and DSTs (ϕ_p^d) are summarized in Table 2.

4.2.1 Effect of sphericity

The peak friction angles ϕ_p and steady friction angles ϕ_s measured in all ISTs are plotted in Fig. 8. Existing research studies reveal that the interface shear strength is profoundly correlated with the shear strength of pure soil. The friction angle measured on a rough IST is close to the friction angle of pure soil [5, 10, 17, 31, 40]. For this reason, the steady friction angles ϕ_s obtained in the numerical ISTs are compared to the critical friction angles ϕ_c of pure soil obtained in the laboratory experiments in Fig. 8b. The experimental databases are derived from the study of Cho et al. [6]. The tested soils include crushed sands and natural sands from various places, and some other materials such as glass beads and granite powder.

Figure 8a shows that the value of ϕ_p increases with the decreasing of the sphericity S when $R_n \geq 0.25$. It implies that the shear strength of SSI is enhanced by the interlocking between interface and particles. This augment due to the particle irregularity is not evident when the specimen

shearing on a relative smooth interface ($R_n = 0.1$). Because in this case, the shear strength at SSI primarily originates from the friction between soil particles and interface. Note that the ϕ_s shows a similar trend for ϕ_p except when S equals 0.7 in the case $R_n = 0.5$, in which the ϕ_s is lower than the one where S equals 0.7. This might be explained by the way the shear stress is not perfectly constant but varies slightly at the steady shear stress state. Moreover, the interaction between two elongated particles ($S = 0.5/0.7$) and the saw-tooth surface is similar, inducing approximate friction angles for the two cases. The evolution trend of ϕ_s at various S is similar to that of the ϕ_c obtained in the laboratory experiment. This result verifies the accuracy of the numerical simulation to a certain degree. It suggests a correlation between the particle sphericity and the friction angle of SSI in the case of relative rough interface.

4.2.2 Effect of interface roughness R_n

The peak friction angle ϕ_p measured on SSI is affected by R_n as well as S as illustrated in Fig. 9. In general, the value of ϕ_p increases as the increasing of R_n. This tendency is valid for the specimens featuring varying sphericity S. To compare the numerical results to the laboratory experiment results, the friction angles ϕ_p measured in IST are normalized by the ϕ_p^d obtained in DST. The ratios of ϕ_p/ϕ_p^d at
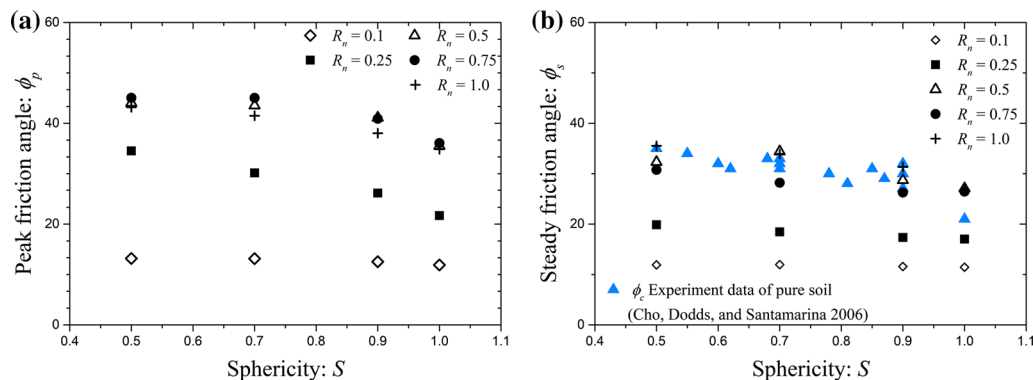

Fig. 8 **a** Peak friction angle ϕ_p obtained in the DEM ISTs; **b** comparison of the steady friction angle ϕ_s obtained in the DEM ISTs to the critical friction angle ϕ_c of pure soil obtained in the laboratory experiments (Cho et al. [6]) at varying sphericity S
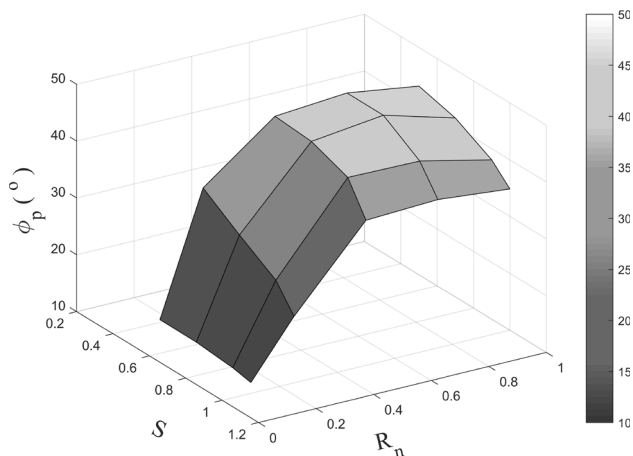
Fig. 9 The peak friction angle ϕ_p at varying normalized roughness of interface R_n and sphericity S
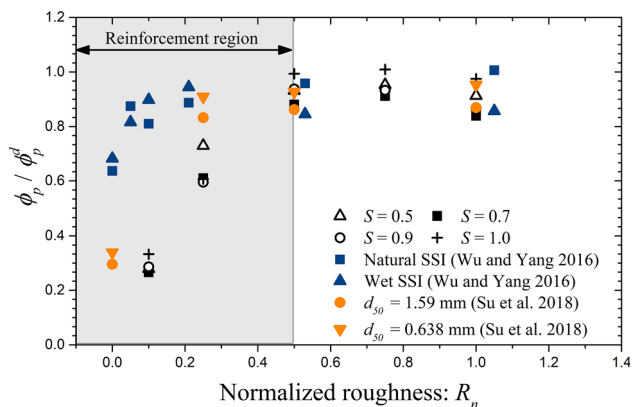

Fig. 10 Comparison of the friction angle ratio ϕ_p/ϕ_p^d obtained in the DEM to those measured in the laboratory experiments [37, 46] at varying normalized roughness R_n of interface

varying R_n are plotted in Fig. 10. The experimental data are derived from the ISTs between natural soil and steel plate [37, 46]. Figure 10 illustrates that the value of ϕ_p/ϕ_p^d increases significantly in the range of R_n between 0 and 0.5. The growing rates of these tests are different, which depend on the properties of soil material, e.g. friction, grading, water content, particle size, particle shape, etc. When the value of R_n is greater than 0.5, the ratios of ϕ_p/ϕ_p^d achieve to a plateau value. It implies that the interaction between particles and interface similar to the interaction among pure particles when ϕ_p/ϕ_p^d is close to 1.0. Note that the ϕ_p/ϕ_p^d of the IST of $R_n = 1.0$ are slightly less than those of $R_n = 0.5$ and 0.75 in the numerical tests. In this case, the bottom particles of approximately uniform distributed sample ($C_n \approx 1.45$) will be trapped in the valley between sawteeth of interface, which weakens the interlocking between particles and interface. In contrast, for the well-graded soil sample ($C_n = 19.2$) used by Wu and Yang [46], the soil

particles can properly fit in the space of rough interface, leading to a stronger interlocking.

4.3 Localized band analysis

Shearing deformation is largely localized in a narrow zone during the shearing process, named the localized band. The localized band can be analyzed by tracing the movements of each particle at a specific stress state. To average the kinematic field, we set certain measuring windows at different heights for the specimen with a dimension of 100 mm × 100 mm × 5 mm (Fig. 11). The average shear displacement in x-direction $\bar{d}_x$ of the elements in each measuring window is calculated.

The values of $\bar{d}_x$ as a function of Z at different shear stress states ($R_n = 0.5$, $\sigma_n = 50$ MPa) are plotted in Fig. 12. Each dot in the figure represents one measurement at a specific height Z. As the shear stress increases, $\bar{d}_x(Z)$ shows a nonlinearity, and an inflection point appears. The phenomenon of stratification becomes more evident at the steady stress state. The shear displacement induced by the interface shearing largely concentrates in the bottom layer of particles adjacent to the interface, named the localized band, rather than in the upper zone separate from the interface. It is consistent with the numerical result regarding the formation of the localized band in 2D/3D DEM simulations [18, 42] as well as the laboratory experiments using image analysis [12].

The inflection point of the curve of $\bar{d}_x(Z)$ at the steady stress state (when $d_s/d_{50} = 3.5$) is used to define the thickness of the localized band δ_h. Spline interpolation is applied to get a smooth $\bar{d}_x$–Z curve $f(Z)$. The first derivative $f'(Z)$ and second derivative $f''(Z)$ are calculated using the finite difference method. The curvature κ of $f(Z)$ is defined by Eq. 2,

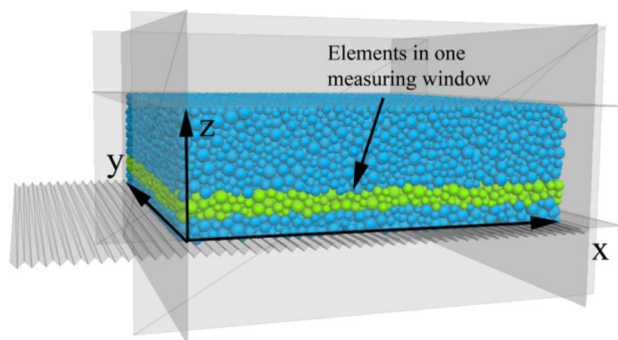$$\kappa = \frac{|f''(Z)|}{\left(1 + f'(Z)^2\right)^{3/2}} \qquad (2)$$

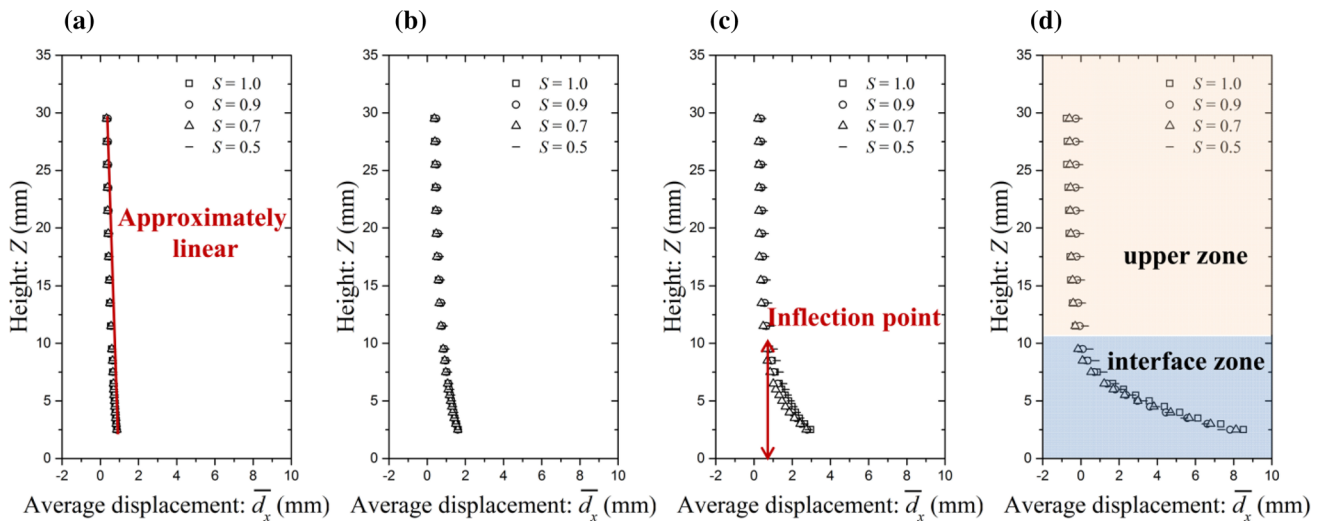**Fig. 11** Set-up of measuring window at different height Z of the specimen

Fig. 12 Average shear displacement in x-direction $\bar{d}_x$ of four ISTs ($R_n = 0.5$, $\sigma_n = 50$ MPa) at different shear states: **a** $d_s = 1.0$ mm; **b** $d_s = 2.0$ mm; **c** $d_s = 4.0$ mm; and **d** $d_s = 13.5$ mm

The $\bar{d}_x$ changes approximately linearly with the height Z toward the higher position of the specimen where the value of κ approaches zero. As Z decreases, the κ sharply increases at a certain value of Z because of the localization of shear deformation. Thus, the inflection point of the κ is considered as a sign of the top boundary of the localized band. Jing et al. [18] suggest that the inflection point is where the κ equals 0.02.

According to this criterion, the thicknesses of the localized band δ_h is rarely affected by the particle sphericity S (Fig. 12). However, Fig. 13 shows that δ_h is affected by R_n and σ_n and it ranges between 0 and 5 times of $d_{50(eq)}$. The localized band is structuralized inside the material when it shearing on a relative rough interface. A thicker localized band is observed in the IST featuring a rougher interface, 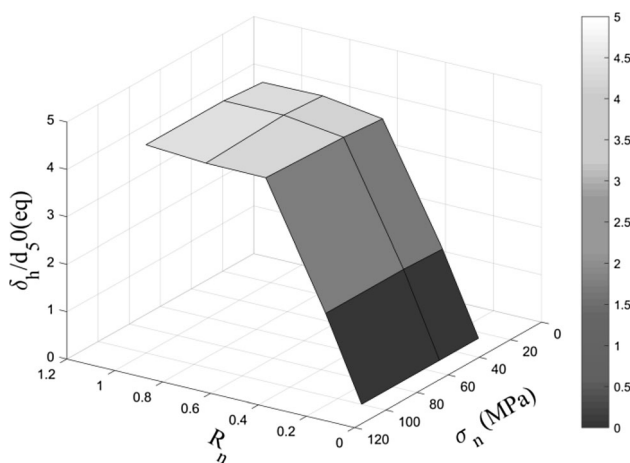which suggests that the failure shifts from the interface into the soil layer. The specimen subjected to a higher normal stress condition ($\sigma_n = 100$ MPa) tends to form a thicker localized band, but the difference is not evident.

4.4 Local porosity and coordination number

To help visualize the local porosity distribution inside the specimen, a grid is constructed to compute the contour of local porosity. Certain measuring balls are set inside the shear box. All the centers of measuring balls are located in the central cross section of shear box, which represent the nodes of the grid. The porosity obtained in each measuring ball represents the local porosity at the position of the center of ball, in another word, the node of grid. Accordingly, the contour of local porosity can be obtained. The contours of local porosity for the IST ($S = 0.7$) at different strain states are plotted in Fig. 14, showing that the initial distribution of porosity is almost homogenous. As shearing progresses, the particles gradually accumulate on the right side and accordingly lead to the dilation on the bottom left corner of the specimen. The dilation region enlarges from the bottom left corner to the bottom part of the entire specimen. The difference in the local porosity inside the specimen reaffirms that the granular material is structuralized into two regions when shearing on an interface (Sect. 4.3). The top line of the localized region is not strictly horizontally straight because of the fixed lateral walls that prevent the movement trend of particles.

The coordination number C_n is used to describe the local contact at particle scale, which is profoundly correlated to the porosity of the granular assembly. It is defined as the average contact number per particle (Eq. 3),
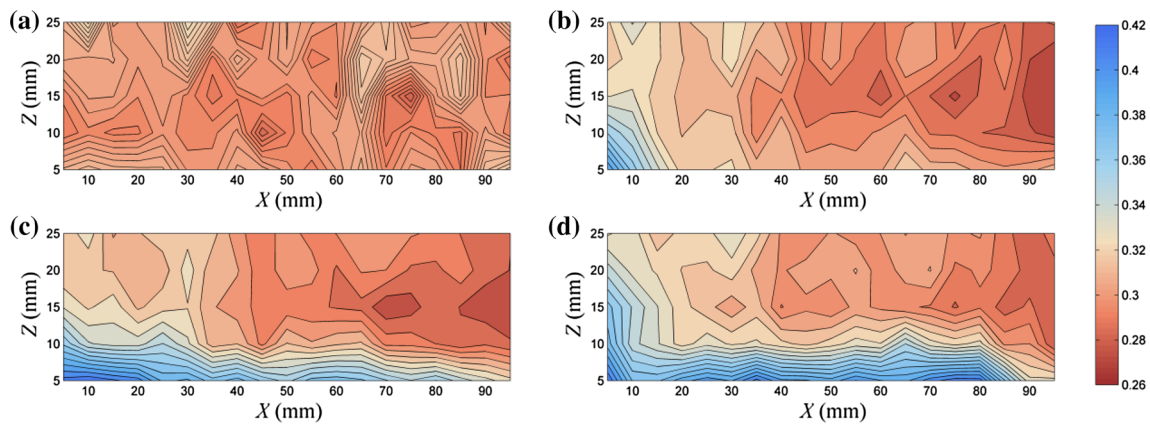

Fig. 13 Normalized thicknesses of localized band $\delta_h/d_{50(eq)}$ of ISTs ($S = 0.5$) at different normal stress σ_n and interface roughness R_n

Fig. 14 Local porosity inside the central section of the specimen ($R_n = 0.5$, $S = 0.7$) at different strain states: **a** $d_s = 0.0$ mm; **b** $d_s = 2.0$ mm; **c** $d_s = 4.0$ mm; and **d** $d_s = 13.5$ mm
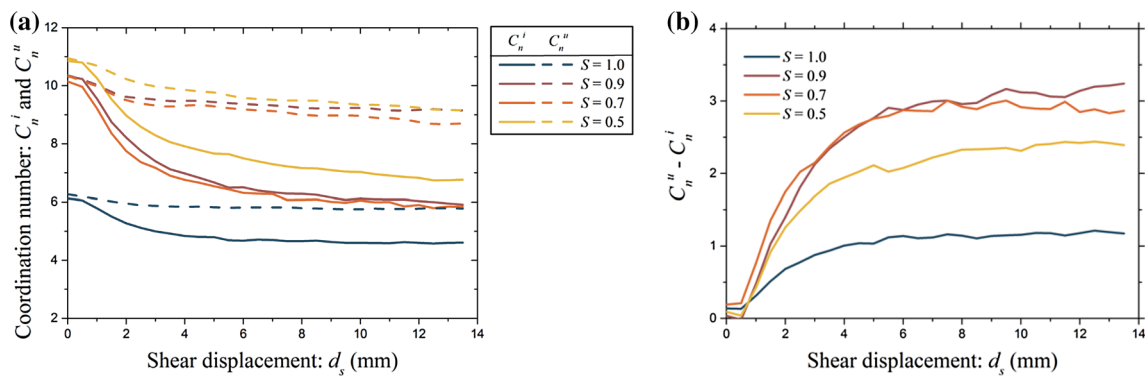

Fig. 15 **a** Coordination number inside the interface zone C_n^i and upper zone C_n^u of the ISTs ($R_n = 0.5$, $\sigma_n = 50$ MPa) with varying sphericity S; **b** the difference between the value measured in interface zone and upper zone $C_n^u - C_n^i$

$$C_n = \left(\sum_{N_p} n_c^p \right) / N_p \qquad (3)$$

where N_p is the total number of particles in the measured region, and n_c^p is the contact number of particles p in the measured region. As discussed in Sect. 4.3, the specimen structuralizes into two regions after shearing, the interface zone and upper zone (Fig. 12d). The evolutions of the coordination number inside the interface zone C_n^i and the upper zone C_n^u for the ISTs with various S are illustrated in Fig. 15a. The initial coordination number of the specimen composed of irregular clumps is much higher than the one consisting of spherical balls, which suggests that more contacts exist between the irregular particles. It explains why interlocking tends to occur inside such granular material. A sharp decrease for C_n^i is observed in all cases; in contrast, the change in C_n^u is minor. The dilation primarily occurs in the interface zone as the contour of local porosity illustrates. The micro-structure of particles in the upper zone is almost preserved. Figure 15b shows the

difference between the values measured in the interface zone and upper zone $C_n^u - C_n^i$. The values of $C_n^u - C_n^i$ increase gradually and approach a steady value. Note that the value in the case of spherical balls is much smaller than the others, in which the total volumetric change is the smallest.

4.5 Material fabric analysis

The macroscopic mechanical behavior of the granular material originates in the distribution and evolution of the material fabric. The distribution of the contact orientation is frequently used to describe the material fabric. A second-order tensor F_{ij} introduced by Satake [35] is used to quantitatively characterize the distribution in normal contact orientation:

$$F_{ij} = \frac{1}{N_c} \sum_{\alpha}^{N_c} n_i^\alpha n_j^\alpha \, (i, j = x, y, z) \qquad (4)$$

where N_c is the total contact number, and n_i is the contact normal vector at contact α. The principal values of F_{ij},

ordered by decreasing magnitude, are F_1, F_2, and F_3. To measure the anisotropy of the material fabric, a deviator fabric δ_D of F_{ij} is calculated as follows Barreto et al. [2]:

$$\delta_D = \frac{1}{\sqrt{2}}\left[(F_1 - F_2)^2 + (F_2 - F_3)^2 + \left(F_1 - F_3\right)^2\right]^{0.5} \quad (5)$$

The evolution of δ_D measured in the interface zone for the ISTs under $\sigma_n = 50$ MPa is plotted in Fig. 16. The initial values of δ_D are slightly higher than zero because anisotropy is induced by the one-dimensional normal pressure before shearing. The δ_D increases with the increasing of shear displacement d_s and decreases once the stress softening appears. The peak value of δ_D depends on particle sphericity. The clumps with smaller sphericity S induce higher anisotropy during the interface sharing, in which a higher interface shear strength is measured. This implies that a correlation exists between δ_D and interface shear strength.

The probability density distribution $P(\vec{n})$ of a unit vector of contact normal $\vec{n}$ is characterized to better visualize the contact distribution inside a granular material. The unit vector $\vec{n}(\theta, \varphi)$ of contact normal between two contacting clumps is obtained based on the spherical coordinate system. The $P(\vec{n})$ can be obtained according to Eq. 6 below

$$P(\vec{n}) = \frac{N_c(d\Omega)}{N_c} \quad (6)$$

where N_c is the total contact number and $N_c(d\Omega)$ is the contact number of contact normal vectors pointing in the direction of a range of angle d_Ω.

The $P(\vec{n})$ measured in the interface zone of the four ISTs at initial state, peak shear stress state, and steady shear stress state are shown in Fig. 17. The shape of $P(\vec{n})$ is close to a spherical ball at the initial state because the specimen is approximately isotropic. As shearing stress increases, the
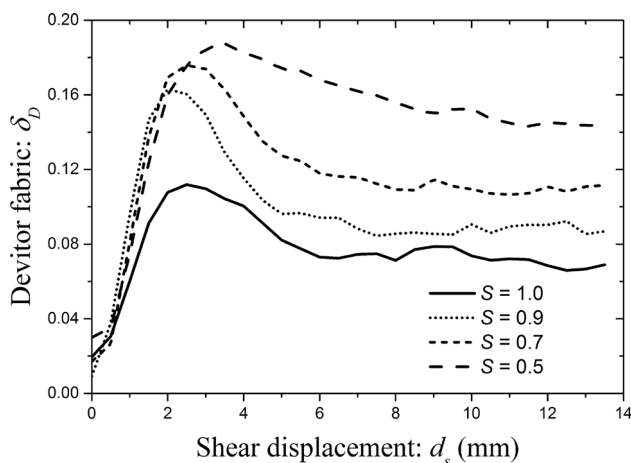
contact orientation gradually accumulates in a certain direction. The concentration of contact orientation is a rearrangement process of particles, increasing the material's anisotropy. The anisotropy at the peak shear stress state is affected by the particle shape, and correspondingly, the shape of $P(\vec{n})$ is different. The anisotropy direction for all the tests featuring various S at peak shear stress state ranges between 40° and 60°. When the shear stress softening occurs and approaches a steady state, the decrease of anisotropy results in the reshaping of $P(\vec{n})$.

5 Effect of initial fabric

In the previous section, the particles were generated randomly inside the shear box, and approximately isotropic specimens were produced. However, the initial material fabric depends upon the initial orientation of the irregular particles, which has an impact on the shearing behavior of SSI. As shown in Fig. 18, θ_p is defined as the included angle between the long axis of the clump and the shear direction (positive x-direction). A specimen consisting of 29,058 clumps featuring $S = 0.7$ with a randomly generated orientation was prepared. In addition, another four specimens were prepared with a given orientation ($\theta_p = 0°/45°/90°/135°$) for each particle. An approximate initial porosity n_0 was controlled for all specimens as listed in Table 3. These specimens sheared on a rough interface featuring R_n equals 0.5 under a normal stress σ_n equals 25/50/100 MPa.

5.1 Macroscopic response

The evolutions of stress ratio τ/σ_n and vertical displacement d_v are illustrated in Fig. 5. The peak shear stress τ_p is affected by the initial orientation of clumps. The specimen consisting of horizontally placed clumps ($\theta_p = 0°$) shows the lowest shearing resistance. As the θ_p increases, the shearing resistance increases. The peak shear stress for the case with randomly distributed clumps is between the extreme cases ($\theta_p = 0°$ and $\theta_p = 135°$). Stress softening is observed among all cases. Moreover, the values of d_s at which the peak shear stress ratio τ_p/σ_n is achieved are different for the five tests. This implies that a different value of d_s is required to fully trigger the interlocking inside the granular materials. Figure 19b illustrates a similar evolutionary trend of volumetric change for various specimens. Before the peak shear stress is achieved, the specimen with an included angle $\theta_p = 135°$ shows the largest dilation; in contrast, the one with horizontally placed clumps dilates less than the others. These results suggest that the vertical movement tends to be easily
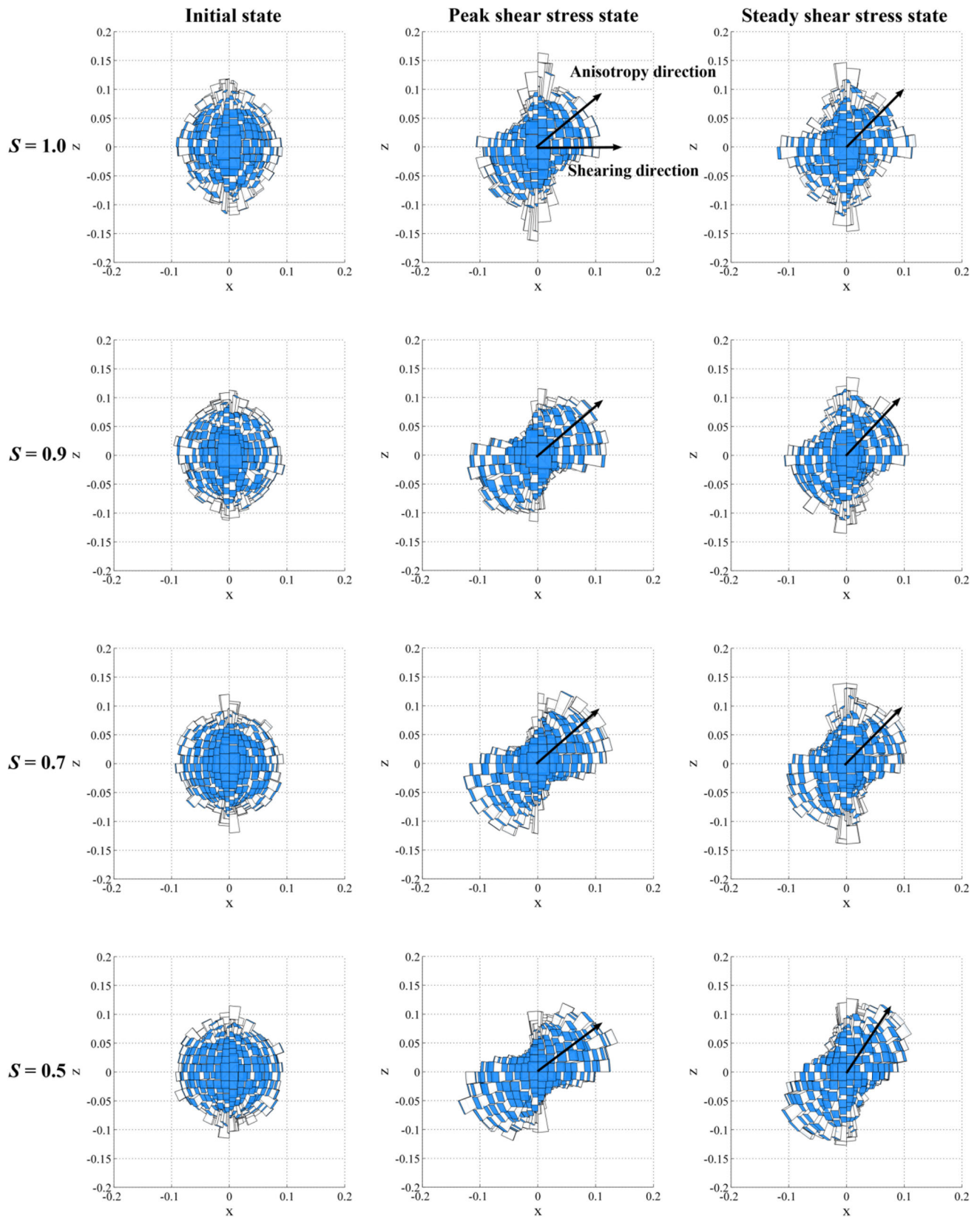
Fig. 16 The evolution of deviator fabric δ_D in the interface zone of the ISTs with various sphericities $S = 1.0/0.9/0.7/0.5$ ($\sigma_n = 50$ MPa, $R_n = 0.5$)

Fig. 17 The contact normal distribution in the interface zone of the four ISTs ($\sigma_n = 50$ MPa, $R_n = 0.5$) at initial state, peak shear stress state, and steady shear stress state
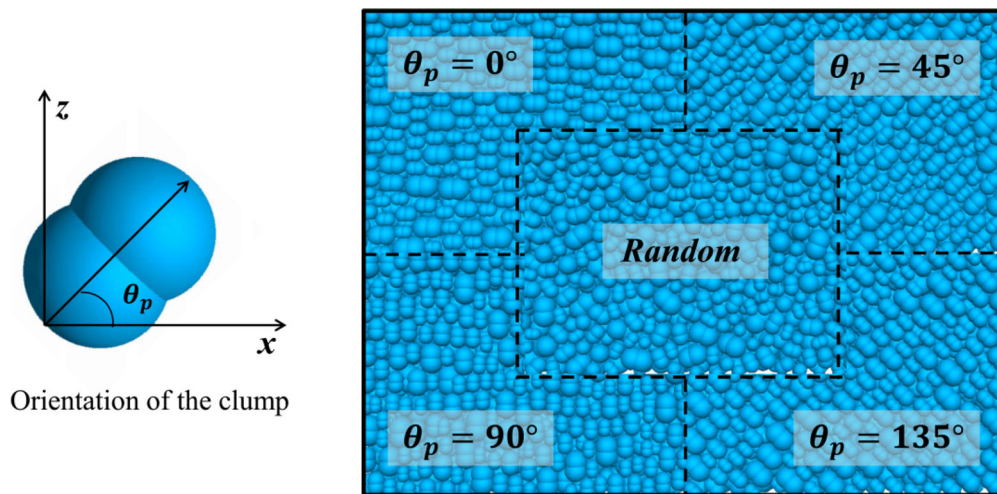
Fig. 18 Five specimens consisting of clumps ($S = 0.7$) with given orientations

triggered when the clumps are randomly placed and $\theta_p = 135°$. In contrast, horizontally placing the clumps restricts the interaction between the bottom layer clumps and the rough interface. Accordingly, both the shear strength and dilatation for that case are the smallest.

5.2 Localized band analysis

The curves of $\bar{d}_x - Z$ for the IST-a/b/c/d/e at different shear stress states are plotted in Fig. 20. The evolution pattern of $\bar{d}_x(Z)$ curves is similar to those of ISTs with varying S. According to the analysis of curvature κ, the thickness of the localized band can be obtained. Figure 21 illustrates the normalized thickness $\delta_h/d_{50(eq)}$ under varying normal stress σ_n, where $d_{50(eq)}$ is the equivalent mean particle diameter. Generally, the $\delta_h/d_{50(eq)}$ is larger when the specimen subjected to a higher σ_n, and the difference induced by confining stress is not evident especially for the cases 25 MPa and 50 MPa. Besides, it shows that the $\delta_h/d_{50(eq)}$ depends on the particle orientation rather than the particle sphericity at the steady stress state. A thicker localized band is formed in the specimen with inclined clumps (i.e. $\theta_p = 45°$ and $135°$) and randomly distributed clumps. It is noted that the value of $\delta_h/d_{50(eq)}$ varies

Table 3 Summary of the numerical tests with various initial fabrics

Test	Clump orientation	Initial porosity: n_0
IST-a	$\theta_p = 0°$	0.337
IST-b	$\theta_p = 45°$	0.335
IST-c	$\theta_p = 90°$	0.339
IST-d	$\theta_p = 135°$	0.336
IST-e	Random	0.338

between 4 and 6, which is slightly higher than that ($\delta_h/d_{50(eq)} = 4$) measured from the previous tests presented in Sect. 4. This is because the n_0 for these tests are relatively higher than the previous ones. The loose specimen tends to form a thicker localized band.

5.3 Local coordination number

The evolutions of coordination number inside the interface zone C_n^i and the upper zone C_n^u for the five ISTs are illustrated in Fig. 22a. The dilation primarily occurs in the interface zone, which is consistent with the tests with varying S (Fig. 15). On the other hand, the C_n^u also decreases during the shearing test; especially in the case $\theta_p = 90°$, it almost decreased the same as the C_n^i. Figure 22b shows the difference between the values measured in the interface zone and upper zone $C_n^u - C_n^i$. The values of $C_n^u - C_n^i$ increase gradually and approach a steady value. It can be noted that the value for case $\theta_p = 90°$ is quite different from the others because the vertically placed clumps are easily disturbed by the shearing even in the upper zone.

5.4 Material fabric analysis

The evolutions of δ_D measured in the interface zone for the ISTs under $\sigma_n = 50$ MPa are plotted in Fig. 23, and the $P(\vec{n})$ at various states are shown in Fig. 24. The specimen consisted of randomly generated clumps, almost isotropic before shearing. Over the progress of shearing, the contacts accumulate in a specific direction, correlated with the shear direction. This anisotropy is purely induced by the shearing, which increases gradually and approaches a peak value at the peak shear stress state. The shear-induced
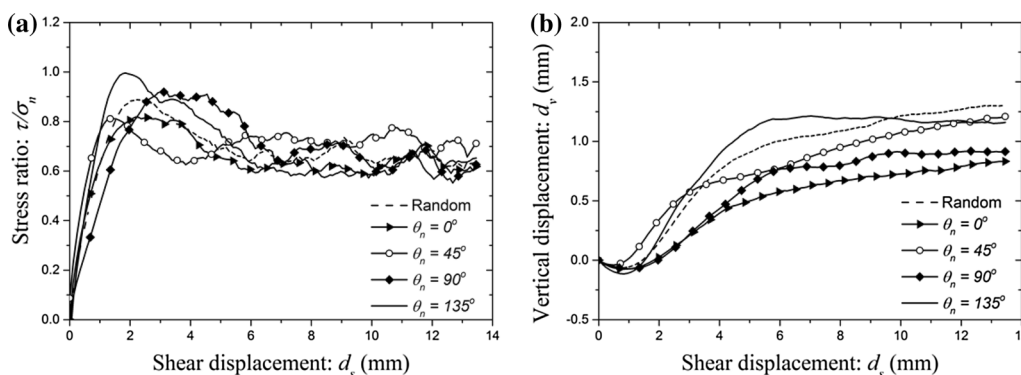
Fig. 19 Macro-responses of the ISTs featuring various included angle θ_p ($\sigma_n = 50$ MPa, $R_n = 0.5$): **a** stress ratio τ/σ_n versus shear displacement d_s; **b** vertical displacement d_v versus shear displacement d_s
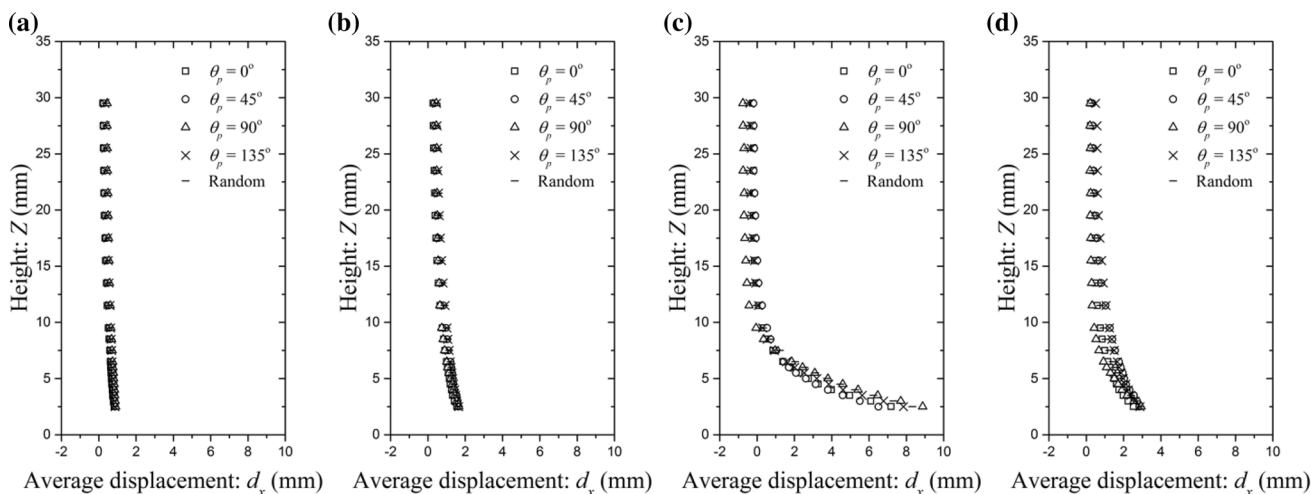

Fig. 20 Average shear displacement in x-direction d_x of five ISTs (random distribution, $\theta_p = 0°/45°/90°/135°$) at different strain states: **a** $d_s = 1.0$ mm; **b** $d_s = 2.0$ mm; **c** $d_s = 4.0$ mm; and **d** $d_s = 13.5$ mm
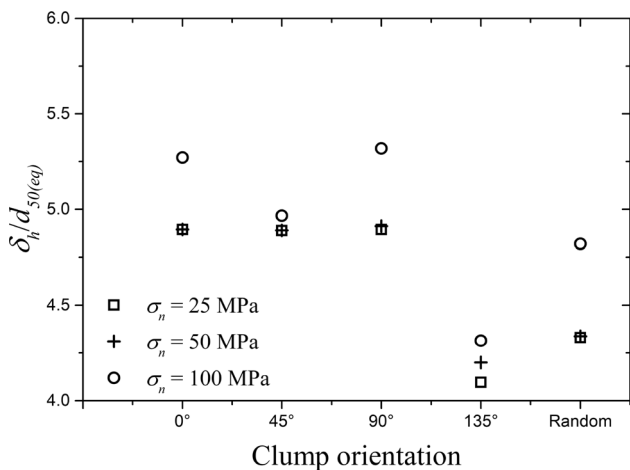

Fig. 21 The normalized thickness of localized band $\delta_h/d_{50(eq)}$ of the specimen comprising of different orientated particles under varying normal stress σ_n

"anisotropy direction" is shown in the figure of $P(\vec{n})$. On the other hand, the initial fabric of specimens consisting of variously oriented particles is anisotropic since the contacts initially concentrated in various directions. The initial anisotropic δ_D for those specimens are about 0.17. As the shear displacement d_s increases, the δ_D increases and then decreases once the stress softening occurs for the cases with $\theta_p = 0°/90°/135°$, as well as the case with a randomly generated specimen. Especially when $\theta_p = 135°$, the contact normal has already been concentrated in the direction of pure shear-induced anisotropy. Thus, the highest level of anisotropy is observed, and accordingly, the largest shearing stress is measured. By contrast, the initial contacts ($\theta_p = 45°$) gather in a direction perpendicular to the pure shear-induced anisotropy direction, preventing the development of the shear-induced anisotropy. For this reason, the δ_D decreases continuously, and a
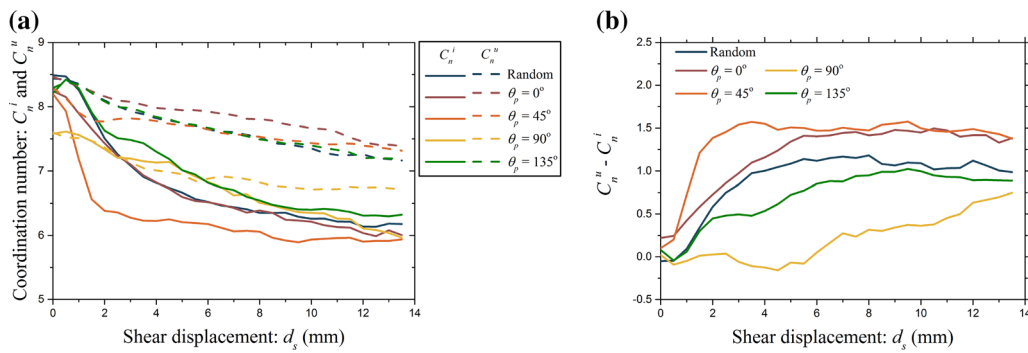
Fig. 22 a Coordination number inside the interface zone C_n^i and upper zone C_n^u of the ISTs ($\sigma_n = 50$ MPa) with differently orientated clumps; **b** the difference between the values measured in the interface zone and upper zone $C_n^u - C_n^i$

minimum peak shear stress is measured. These results demonstrate that the evolution of $P(\vec{n})$ of an anisotropic specimen is profoundly correlated with the "shear-induced anisotropy direction" in the isotropy specimen.

6 Conclusions

The macro- and micro-shearing behaviors of a soil-structural interface have been studied using 3D DEM simulations of ISTs that feature varying sphericity S, interface roughness R_n and initial fabric. The effects of S and σ_n on shear strength, volumetric changes, thickness of the localized band, local porosity, contact normal distribution, and material fabric anisotropy have been analyzed. The following conclusions are drawn.

1. Particle sphericity S plays a significant role in the mechanical properties of the SSI. The shear strength of the interface (i.e. τ_p/σ_n, ϕ_p and ϕ_s) increases as S decreases. The volumetric change in the specimen also
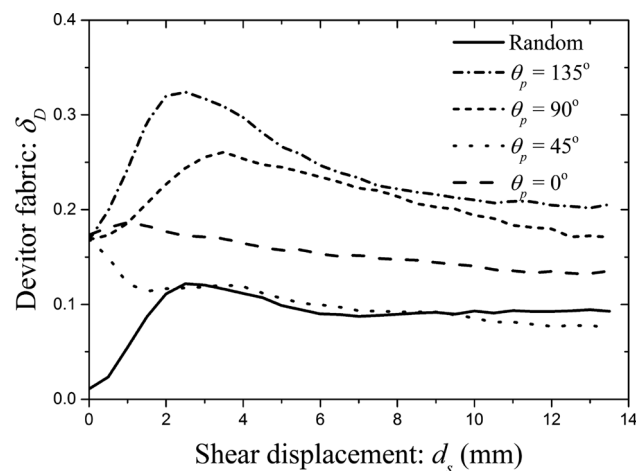

Fig. 23 The evolution of deviator fabric δ_D in the interface zone of five ISTs (random, $\theta_p = 0°/45°/90°/135°$) under $\sigma_n = 50$ MPa and $R_n = 0.5$

depends on S. A larger dilation is observed for the specimen composed of non-spherical particles. The granular material structuralizes into two regions during interface shearing: the interface zone and the upper zone. Anisotropy in the interface zone is increased and a higher deviator fabric δ_D is induced by shearing when S is smaller.

2. The interface roughness R_n affects the shearing behavior of interface. The interface friction angle ϕ_p ascends with the increasing of R_n and reaches to a plateau value. The growing rate is associated with the particle sphericity S. A thicker localized band is observed in the IST featuring a rougher interface.

3. The shear strength of the interface is affected by the initial fabric (particle orientation) of the specimen. The peak shear stress increases as the particle orientation increases. The initial fabric is associated with the interaction between the particles and rough interface, i.e., restricts or triggers the motions of particles. The specimen with an inclined angle $\theta_p = 135°$ shows the largest dilation; in contrast, the one with horizontally placed clumps dilates less than the others. The thickness of the localized band δ_h depends on the initial fabric. A thicker localized band is formed in a specimen with inclined clumps ($\theta_p = 45/135°$) and randomly distributed clumps. This tendency is generally valid under varying normal stress conditions. The given particle orientation leads to the different initial fabric of the specimen. The initial fabric affects the evolution of $P(\vec{n})$ and δ_D.

It is noted that this study has only examined the effect of sphericity S of irregular particles. Particle shape in nature is more random and complicated. To extend the study, other shape parameters should be considered in the future. Despite these limitations, this study clearly indicates the significant effect of S and its correlation with interface shear strength. The analysis of the micro-quantities, including the contact normal distribution, the motion of the
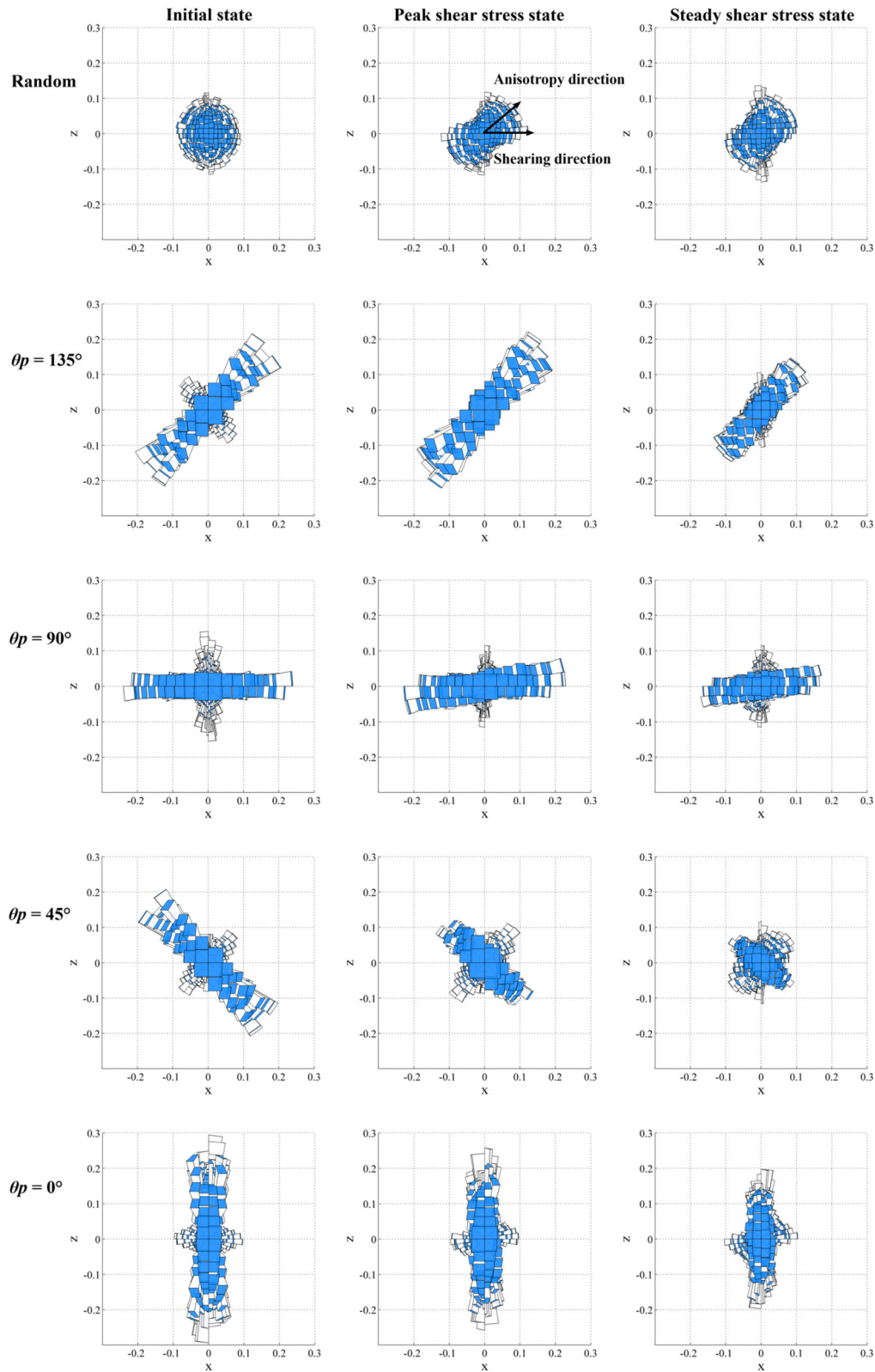
Fig. 24 The contact normal distribution in the interface zone of the five ISTs (random, $\theta_p = 0°/45°/90°/135°$) under $\sigma_n = 50$ MPa and $R_n = 0.5$ at initial state, peak shear stress state, and steady shear stress state

particle, and the local porosity distribution, improves our understanding of the micro-mechanisms associated with soil-interface shearing.

References

1. Ai J, Chen JF, Rotter JM, Ooi JY (2011) Assessment of rolling resistance models in discrete element simulations. Powder Technol 206(3):269–282
2. Barreto D, O'Sullivan C, Zdravkovic L (2009) Quantifying the evolution of soil fabric under different stress paths. In: AIP conference proceedings, London, pp 181–84
3. Bono JP, Mcdowell GR (2015) An insight into the yielding and normal compression of sand with irregularly-shaped particles using DEM. Powder Technol 271:270–277
4. Chang CS, Yin ZY (2009) Micromechanical modeling for inherent anisotropy in granular materials. J Eng Mech 136(7):830–839
5. Chen X, Zhang J, Xiao Y, Li J (2015) Effect of roughness on shear behavior of red clay—concrete interface in large-scale direct shear tests. Can Geotech J 52(8):1122–1135
6. Cho GC, Dodds J, Santamarina JC (2006) Particle shape effects on packing density, stiffness and strength: natural and crushed sands. J Geotech Geoenviron Eng 132(5):591–602
7. Coetzee CJ (2016) Calibration of the discrete element method and the effect of particle shape. Powder Technol 297:50–70
8. Cundall PA, Strack ODL (1979) A discrete numerical model for granular assemblies. Géotechnique 29(1):47–65
9. Dejong JT, White D, Randolph MF (2006) Microscale observation and modeling of soil-structure interface behavior using particle image. Soils Found 46(1):15–28
10. Frost JD, Dejong JT, Recalde M (2002) Shear failure behavior of granular-continuum interfaces. Eng Fract Mech 69(17):2029–2048
11. Hossain MA, Yin JH (2014) Behavior of a pressure-grouted soil-cement interface in direct shear tests. Int J Geomech 14(1):101–109
12. Hu LM, Pu JL (2005) Testing and modeling of soil-structure interface. J Geotech Geoenviron Eng 130(8):851–860
13. Iwashita K, Oda M (1998) Rolling resistance at contacts in simulation of shear band development by DEM. J Eng Mech 124(3):285–292
14. Jensen RP, Bosscher PJ, Plesha ME, Edil TB (1999) DEM simulation of granular media-structure interface: effects of surface roughness and particle shape. Int J Numer Anal Meth Geomech 23(6):531–547
15. Jiang M, Yin ZY (2012) Analysis of stress redistribution in soil and earth pressure on tunnel lining using the discrete element method. Tunn Undergr Space Technol 32:251–259
16. Jiang M, Yin ZY (2014) Influence of soil conditioning on ground deformation during longitudinal tunneling. CR Mec 342(3):189–197
17. Jing XYWH, Zhou HXZhu, Yin ZY (2018) Analysis of soil-structural interface behavior using three-dimensional DEM simulations. Int J Numer Anal Meth Geomech 42(2):339–357
18. Jing XY, Zhou WH, Li YM (2017) Interface direct shearing behavior between soil and saw-tooth surfaces by DEM simulation. Procedia engineering. Delft, The Netherlands, pp 36–42
19. Krumbein WCh, Sloss LL (1951) Stratigraphy and sedimentation. LWW
20. Lin X, Ng TT (1997) A three-dimensional discrete element model using arrays of ellipsoids. Géotechnique 47(2):319–329
21. Lu M, Mcdowell GR (2007) The importance of modelling ballast particle shape in the discrete element method. Granular Matter 9(1–2):69–80
22. Mindlin RD, Deresiewicz H (1953) Elastic spheres in contact under varying oblique forces. J Appl Mech 20:327–344
23. Miura K, Maeda K, Furukawa M, Toki S (1998) Mechanical characteristics of sands with different primary properties. Soils Found 38(4):159–172
24. Nakata Y et al (2001) One-dimensional compression behaviour of uniformly graded sand related to single particle crushing strength. Soils Found 41(2):39–51
25. Ni Q, Powrie W, Zhang X, Harkness R (2000) Effect of particle properties on soil behavior: 3-D numerical modeling of shearbox tests. In: Numerical methods in geotechnical engineering, ASCE Geotechnical Special Publication, pp 58–70
26. Ochiai H, Otani J, Hayashic S, Hirai T (1996) The pull-out resistance of geogrids in reinforced soil. Geotext Geomembr 14(1):19–42
27. Oda M, Nemat-Nasser S, Konishi J (1985) Stress-induced anisotropy in granular masses. Soils Found 25(3):85–97
28. Paikowsky SG, Player CM, Connors PJ (1995) A dual interface apparatus for testing unrestricted friction of soil along solid surfaces. ASTM Geotech Test J 18(2):168–193
29. Peng SY, Ng CWW, Zheng G (2014) The dilatant behaviour of sand-pile interface subjected to loading and stress relief. Acta Geotech 9(3):425–437
30. Pra-ai S, Boulon M (2017) Soil-structure cyclic direct shear tests: a new interpretation of the direct shear experiment and its application to a series of cyclic tests. Acta Geotech 12(1):107–127
31. Rao KSS, Allam MM, Robinson RG (1998) Interfacial friction between sands and solid surfaces. In: Proceedings of the ICE–geotechnical engineering, pp 75–82
32. Rothenburg L, Bathurst RJ (1992) Micromechanical features of granular assemblies with planar elliptical particles. Géotechnique 42(1):79–95
33. Salot C, Gotteland P, Villard P (2009) Influence of relative density on granular materials behavior: DEM simulations of triaxial tests. Granular Matter 11(4):221–236
34. Santamarina JC, Cho GC (2004) Soil behaviour: the role of particle shape. In: Advances in geotechnical engineering: the Skempton conference, London, pp 604–17
35. Satake M (1992) A discrete-mechanical approach to granular materials. Int J Eng Sci 30(10):1525–1533
36. Su LJ, Yin JH, Zhou WH (2010) Influences of overburden pressure and soil dilation on soil nail pull-out resistance. Comput Geotech 37(4):555–564
37. Su LJ, Zhou WH, Chen WB, Jie X (2018) Effects of relative roughness and mean particle size on the shear strength of sand-steel interface. Measurement 122:339–346
38. Uesugi M, Kishida H (1986) Frictional resistance at yield between dry sand and mild steel. Soils Found 26(4):139–149
39. Uesugi M, Kishida H (1986) Influential factors of friction between steel and dry sands. Soils Found 26(2):33–46
40. Uesugi M, Kishida H, Tsubakihara Y (1988) Behavior of sand particles in sand-steel friction. Soils Found 28(1):107–118
41. Wang HL, Chen RP, Liu QW, Kang X, Wang YW (2019) Soil–geogrid interaction at various influencing factors by pullout tests

with applications of FBG sensors. J Mater Civil Eng 31(1):04018342

42. Wang J, Gutierrez MS, Dove JE (2007) Numerical studies of shear banding in interface shear tests using a new strain calculation method. Int J Numer Anal Meth Geomech 31(12):1349–1366

43. Wang J, Jiang M (2011) Unified soil behavior of interface shear test and direct shear test under the influence of lower moving boundaries. Granular Matter 13(5):631–641

44. Wensrich CM, Katterfeld A (2012) Rolling friction as a technique for modelling particle shape in DEM. Powder Technol 217:409–417

45. Wood DM, Maeda K (2007) Changing grading of soil: effect on critical states. Acta Geotech 3(1):3–14

46. Wu XY, Yang J (2016) Direct shear tests of the interface between filling soil and bedrock of Chongqing airport. In: Advances in civil, envrionmental, and materials research (ACEM16), Jeju Island

47. Yin JH, Zhou WH (2009) Influence of grouting pressure and overburden stress on the interface resistance of a soil nail. J Geotech Geoenviron Eng 135(9):1198–1208

48. Yin ZY, Chang CS, Hicher PY (2010) Micromechanical modelling for effect of inherent anisotropy on cyclic behaviour of sand. Int J Solids Struct 47(14):1933–1951

49. Zhao LS, Zhou WH, Yuen KV (2017) A simplified axisymmetric model for column supported embankment systems. Comput Geotech 92:96–107

50. Zhou J, Gong X, Wang K, Zhang R (2018) Shaft capacity of the pre-bored grouted planted pile in dense sand. Acta Geotech 13(5):1227–1239

51. Zhou WH, Yin JH (2008) A simple mathematical model for soil nail and soil interaction analysis. Comput Geotech 35(3):479–488

52. Zhou WH, Yin JH, Hong CY (2011) Finite element modelling of pullout testing on a soil nail in a pullout box under different overburden and grouting pressures. Can Geotech J 48(4):557–567

53. Zhou WH, Yuen KV, Tan F (2013) Estimation of maximum pullout shear stress of grouted soil nails using bayesian probabilistic approach. Int J Geomech 13(5):659–664

54. Zhu HX, Zhou WH, Yin ZY (2018) Deformation mechanism of strain localization in 2D numerical interface tests. Acta Geotech 13:557–573